PCCP

ROYAL SOCIETY OF CHEMISTRY

PAPER

View Article Online
View Journal | View Issue

Check for updates

Cite this: *Phys. Chem. Chem. Phys.*, 2025, **27**, 4704

# Local order, disorder, and everything in between: using $^{91}$Zr solid-state NMR spectroscopy to probe zirconium-based metal–organic frameworks†

Wanli Zhang,[a] Bryan E. G. Lucier,[a] Vinicius Martins,[a] Tahereh Azizivahed,[a] Ivan Hung,[b] Yijue Xu,[b] Zhehong Gan,[b] Amrit Venkatesh,[bcd] Tian Wei Goh,[cd] Wenyu Huang,[cd] Aaron J. Rossini[cd] and Yining Huang *[a]

Received 25th September 2024,
Accepted 30th January 2025

DOI: 10.1039/d4cp03704a

rsc.li/pccp

Characterization of metal centers in metal–organic frameworks (MOFs) is critical for rational design and further understanding of structure–property relationships. The short-range structure about Zr atoms is challenging to properly elucidate in many Zr MOFs, particularly when local disorder is present. Static $^{91}$Zr solid-state NMR spectra of the seven zirconium MOFs UiO-66, UiO-66-NH$_2$, UiO-67, MOF-801, MOF-808, DUT-68 and DUT-69 have been acquired at high magnetic fields of 35.2 T and 19.6 T, yielding valuable information on the local structure, site symmetry and order about Zr. $^{91}$Zr NMR is very sensitive to differences in MOF short-range structure caused by guest molecules, linker substitution and post-synthetic treatment. Complementary density functional theory (DFT) calculations assist in the interpretation and assignment of $^{91}$Zr solid-state NMR spectra, lend insight into structural origins of $^{91}$Zr NMR parameters and enable determination of local Zr coordination environments. This approach can be extended to many other materials containing zirconium.

## Introduction

Metal–organic frameworks (MOFs) are hybrid materials composed of metal centers or metal-based clusters connected by organic linkers. This class of compounds has many applications, including in the fields of catalysis, gas storage, gas separation and energy storage.[1] MOFs are composed of crystalline one-, two-, or three-dimensional structures, and the accompanying high degree of long-range order typically allows for straightforward structural determination *via* X-ray or neutron diffraction-based experiments. MOFs often harbor various types of short-range disorder that is difficult to investigate using diffraction-based crystallographic methods, including local compositional variations, positional disorder, atomic displacements, defect sites, and dynamic guests;[2] many of these modes of disorder are present in Zr MOFs.[3–5] When a crystal used in X-ray diffraction is not perfectly ordered, the amount of chemical disorder can be quantified by the fractional occupancy and/or anisotropic atomic displacement, but these values only reflect average disorder across the entire long-range ordered structure and cannot offer short-range insight.[6] Solid-state NMR spectroscopy is an excellent complementary tool to diffraction, as it is very sensitive to the local environment around the nucleus and is applicable to disordered systems.[6–8]

Zirconium-based MOFs are particularly attractive due to their high chemical stability, structural tunability, and diverse potential applications.[9] For example, the UiO-66 MOF has demonstrated excellent catalytic performance for many reactions,[10,11] and its structure can also be tailored through defect engineering.[12] A common strategy to obtain highly crystalline Zr-MOFs involves the use of a modulation agent during synthesis;[9] however, modulators typically produce structures with short-range disorder about the metal centers and organic linkers.[3–5] The metal centers in MOFs play crucial roles in many applications; thus, fully understanding the short-range structure and local order around the metal is crucial for rational design of MOFs tailored for specific applications.[13]

Solid-state NMR spectroscopy has proven useful for investigating the local structures around metal ions in MOFs.[14–18] Most NMR-active metal isotopes are quadrupolar nuclei and are intrinsically insensitive, including $^{91}$Zr. The only NMR-active Zr isotope, $^{91}$Zr (spin 5/2), has a very low magnetogyric ratio ($\gamma$) of $-2.49750 \times 10^{7}$ rad T$^{-1}$ s$^{-1}$,[19] a low natural isotope abundance of 11.23%,[20] and a moderate quadrupole moment

---

[a] *Department of Chemistry, University of Western Ontario, London, Ontario, N6A 5B7, Canada. E-mail: yhuang@uwo.ca*
[b] *National High Magnetic Field Laboratory, 1800 East Paul Dirac Drive, Tallahassee, Florida 32310, USA*
[c] *U.S. Department of Energy Ames National Laboratory, Ames, Iowa 50011, USA*
[d] *Department of Chemistry, Iowa State University, Ames, Iowa 50011, USA*
† Electronic supplementary information (ESI) available. See DOI: https://doi.org/10.1039/d4cp03704a

$Q(^{91}Zr) = -0.176$ (barn);[21] these properties often give rise to broad $^{91}$Zr solid-state NMR spectra with low signal-to-noise ratios that are challenging to acquire.[22] MOF unit cells are typically large, resulting in significant weight dilution of Zr metal centers. The reduced density of $^{91}$Zr spins poses an additional challenge for acquisition of $^{91}$Zr solid-state NMR spectra at natural isotopic abundance. Due to these unfavorable conditions, there have been only three successful reported $^{91}$Zr solid-state NMR experiments on MOFs.[4,16,23]

Despite the multiple challenges associated with $^{91}$Zr NMR spectroscopy, this route has the potential to provide a wealth of information on the short-range metal environments in Zr-MOFs. The $Q$ interacts with the electric field gradient (EFG) surrounding Zr in a process known as the quadrupolar interaction (QI). The QI is very sensitive to the local structure because, while $Q$ is a constant, the EFG arises from the surrounding electronic environment. The quadrupolar coupling constant ($C_Q$) and the asymmetry parameter ($\eta_Q$) are used to describe the QI. A higher $C_Q$ value corresponds to a larger EFG and a less symmetric local environment; larger $C_Q$ values give rise to broader $^{91}$Zr solid-state NMR spectra that are more challenging to collect. The $\eta_Q$ value ranges from zero to one and reflects the axial symmetry of the EFG tensor; by extension, $\eta_Q$ quantifies the local axial symmetry of the EFG about Zr. A lower $\eta_Q$ corresponds to a more axially symmetric environment. $^{91}$Zr solid-state NMR spectra are also influenced to a lesser degree by the chemical shift (CS) interaction, particularly the isotropic chemical shift ($\delta_{iso}$),[24] although the $^{91}$Zr solid-state NMR spectrum of UiO-66_Ac30 at 35.2 T in this work illustrates how chemical shift anisotropy (CSA) can have some impact.

The development of NMR instruments with high magnetic fields ($>$18.8 T) in recent decades have rendered solid-state NMR of unreceptive nuclei feasible, including $^{91}$Zr. Higher magnetic fields enhance the inherent sensitivity of the NMR experiment and also significantly reduce spectral line broadening associated with quadrupolar nuclei, as the second-order QI is inversely proportional to the magnetic field strength. Leveraging these advantages, high-field $^{91}$Zr solid-state NMR spectroscopy has been used to investigate ordered materials such as zirconium halides, zirconium phosphates, and zirconocenes.[23–29] The quadrupolar Carr–Purcell Meiboom–Gill (QCPMG)[30] pulse sequence has also proven useful for acquiring NMR spectra of insensitive quadrupolar nuclei such as $^{91}$Zr.[31] Despite the vast potential of $^{91}$Zr solid-state NMR spectroscopy, molecular-level characterization of Zr-based MOFs is rare and often challenging.[4,16,23]

$^{91}$Zr solid-state NMR spectroscopy at high magnetic fields of 35.2 and 19.6 T has been used to characterize several representative Zr-MOFs, with the results also providing insights into the local disorder known to exist in such systems.[2] The well-known UiO-66 and UiO-67 MOFs are first examined, revealing a lower rotational site symmetry around Zr than was indicated from the single crystal structure. The impact of missing-linker defects in UiO-66 MOFs is characterized. The origins and effects of linker-related disorder are probed in the UiO-66-NH$_2$ MOF. Using MOF-801, we then show how $^{91}$Zr NMR spectroscopy can be used to monitor the Zr local environment during thermal activation of a MOF. Chemical-induced changes in the Zr local structure are explored in the post-acidification treatment of MOF-808. Finally, the influence of a synthesis modulator on local order and structure is illustrated using the DUT-68 and DUT-69 MOFs. DFT calculations can provide detailed insight into the origin of QI parameters; we have performed calculations using plane-wave DFT and cluster DFT approaches that shed light on the structural origins of these $^{91}$Zr NMR spectra (Fig. S9 and Table S2, ESI†).

## Results and discussion

UiO-66 was first reported in 2008 and is one of the most well-known and widely studied Zr-MOFs.[32] This material has exhibited exceptional tunability and can incorporate various chemical functionalities,[10] which is promising for applications in fields such as gas adsorption, gas separation, catalysis, and chemical sensing.[10,12] The structure of UiO-66 was initially solved using powder X-ray diffraction (PXRD),[32] and later by single crystal XRD.[33] UiO-66 resides in the $Fm\bar{3}m$ space group, with the zirconium-oxo secondary building units (SBUs) occupying the vertices and face-centered locations in the cubic unit cell (Fig. 1(a)); the SBUs are connected by benzene-1,4-dicarboxylate (BDC) linkers. Each Zr is coordinated to eight oxygen atoms, where the four oxygens termed O1 originate from four separate BDC linkers and the other four O2 oxygens are $\mu_3$-O atoms from $O^{2-}$ and $OH^-$ groups. SCXRD experiments[33] revealed that the $\mu_3$-O site is disordered with a 0.5 fractional occupancy in both possible positions ($O2^i$ and $O2^{ii}$), while Zr possesses local $C_4$ rotational symmetry.

The static $^{91}$Zr solid-state NMR spectra of as-made and activated UiO-66 acquired at 35.2 T are shown in Fig. 1(b). Thermal activation of UiO-66 was carried out to remove water from the pores of the MOF, which was confirmed by $^1H$–$^{13}C$ CP/

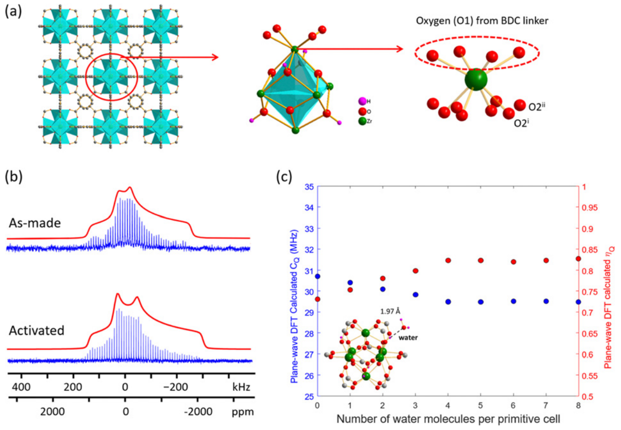

Fig. 1 (a) The long-range structure of UiO-66, along with the local structure about Zr from single crystal XRD.[33] (b) Experimental (blue) and simulated (red) static $^{91}$Zr QCPMG solid-state NMR spectra of as-made and activated UiO-66 obtained at a magnetic field of 35.2 T. (c) $C_Q$ and $\eta_Q$ values calculated using plane-wave DFT plotted *versus* the number of water molecules incorporated in each primitive cell. The activated structure has zero water molecules per primitive cell, while the as-made structure features eight water molecules per cell.

MAS and $^{1}$H MAS NMR experiments (Fig. S2, ESI†). The spectrum of activated UiO-66 features a relatively well-defined QI-dominated powder pattern corresponding to a $C_Q(^{91}\text{Zr})$ of 35.5(3) MHz, $\eta_Q$ of 0.78(3), and $\delta_{\text{iso}}$ of −150(50) ppm (Table 1). The intensity of the experimental NMR spectrum at lower frequencies (*i.e.*, lower ppm values) is slightly less in comparison to analytical simulations. This difference can be attributed to imperfections in the rf pulses (see numerical simulations, Fig. S10, ESI†), anisotropy of the spin echo transverse relaxation times $\left(T_2'\right)$ across the frequency range, and local disorder. The non-zero $\eta_Q$ indicates that there cannot be $\geq C_3$ rotational symmetry at Zr, which conflicts with the reported $C_4$ rotational symmetry.[33] The possible positions for the two $O^{2-}$ and two $OH^{-}$ groups (O2$^{\text{i}}$ and O2$^{\text{ii}}$, Fig. 1(a), occupancies of 0.5 each) lead to four possible oxygen structural configurations about Zr in line with the $Fm\bar{3}m$ space group (Fig. S11, ESI†): (1) two $O^{2-}$ and two $OH^{-}$ groups occupy O2$^{\text{i}}$; (2) two $O^{2-}$ and two $OH^{-}$ groups occupy O2$^{\text{ii}}$; (3) two $OH^{-}$ groups are located at O2$^{\text{i}}$ and two $O^{2-}$ groups are located at O2$^{\text{ii}}$; (4) two $OH^{-}$ groups are located at O2$^{\text{ii}}$ and two $O^{2-}$ groups are located at O2$^{\text{i}}$. If all instances are equally probable, the experimental $^{91}$Zr NMR spectrum should be composed of contributions from all four possible configurations.

Table 1 Experimental and DFT-calculated $^{91}$Zr NMR parameters

| | $\delta_{\text{iso}}$ (ppm) | $C_Q$ (MHz) | $\eta_Q$ | $\epsilon$ | Source of local disorder at Zr |
|---|---|---|---|---|---|
| UiO-66 (as made) | | | | | |
| Experimental | −100(50) | 31.5(3) | 0.85(3) | 0.00(5)[b] | — |
| Plane-wave DFT | −309 | 29.5 | 0.82 | — | — |
| Cluster DFT | −46 | 28.5 | 0.92 | — | — |
| UiO-66 (activated) | | | | | |
| Experimental | −150(50) | 35.5(3) | 0.78(3) | 0.00(5)[b] | — |
| Plane-wave DFT | −286 | 30.7 | 0.73 | — | — |
| Cluster DFT | −34 | 29.1 | 0.58 | — | — |
| UiO-66_Ac30 (activated)[a] | | | | | |
| Experimental | −100(30) | 32.5(3) | 0.79(3) | 0.00(5)[b] | — |
| UiO-67 (as made) | | | | | |
| Experimental | −20(30) | 23.2(7) | 0.91(3) | 0.00(5)[b] | — |
| Plane-wave DFT | −286 | 28.9 | 0.73 | — | — |
| Cluster DFT | −39 | 25.3 | 0.92 | — | — |
| UiO-66-$NH_2$ (activated) | | | | | |
| Experimental | 150(20) | 26.5(8) | 0.72(5) | 0.60(6) | BDC-$NH_2$ linker |
| Plane-wave DFT[c] | −236 | 29.6 | 0.75 | — | — |
| Cluster DFT[c] | −39 | 30.6 | 0.63 | — | — |
| MOF-808 (activated) | | | | | |
| Experimental | 80(10) | 18.4(5) | 0.90(3) | 0.07(2) | $HCOO^{-}$ ions |
| Plane-wave DFT | 176 | 16.6 | 0.86 | — | — |
| Cluster model | −53 | 17.6 | 0.89 | — | — |
| MOF-808-1.3$SO_4$ (as made) | | | | | |
| Experimental | 50(10) | 17.0(5) | 0.72(4) | 0.35(4) | $SO_4^{2-}$ ions |
| MOF-801 (as-made) | | | | | |
| Experimental | 0(50) | 20.0(6) | 0.90(3) | 0.10(3) | $H_2O$ molecules |
| Cluster model | −9 | 26.6 | 0.84 | — | — |
| MOF-801 (activated) | | | | | |
| Experimental/site 1 | 0(40) | 29.0(10) | 0.65(3) | 0.00(5)[b] | — |
| Experimental/site 2 | 0(50) | 20.0(6) | 0.90(4) | 0.10(3) | $H_2O$ molecules |
| Plane-wave DFT | −221 | 30.8 | 0.64 | — | — |
| Cluster model | −8 | 31.2 | 0.50 | — | — |
| DUT-68 (as made) | | | | | |
| Experimental | −38.0(10) | 14.9(6)[d] | N/A | — | Zr-oxo clusters in pore |
| DUT-69 (as made) | | | | | |
| Experimental/site 1 | 150(20) | 18.5(3) | 0.38(2) | — | — |
| Experimental/site 2 | 0(20) | 19.1(4) | 0.85(3) | — | — |

[a] Simulations for UiO-66_Ac30 included CSA parameters as indicated in Fig. 2. [b] In these simulations, a value of 0 was used for $\epsilon$, and the uncertainty in this parameter was determined to be no larger than 0.05. [c] The DFT calculations were performed on the structure with minimal energy, and the averaged values from plane-wave and cluster DFT calculations are listed here (details in Table S3, ESI). [d] The Czjzek model was used for this simulation, and the resulting $\sqrt{\langle C_Q{}^2 \rangle}$ value is listed here. Please refer to the SI for a more detailed description of the Czjzek and extended Czjzek models.

Using the four possible oxygen configurations in UiO-66 as starting points, plane-wave DFT geometry optimizations were performed on all atoms in the four structures. Geometry optimization using all four possible configurations as a starting point yielded the same outcome: the $O^{2-}$ groups move to the $O2^{i}$ sites, while the $OH^{-}$ groups move to the $O2^{ii}$ sites, in an outcome resembling the aforementioned situation (4). Plane-wave DFT calculations produced a $C_Q(^{91}Zr)$ of 30.7 MHz and $\eta_Q$ of 0.73 in all cases, which were in good agreement with experimental findings. The optimized structure featured a Zr–$OH^{-}$ (Zr–$O2^{ii}$) bond length of 2.265 Å, which is considerably longer than the Zr–$O^{2-}$ (Zr–$O2^{i}$) length of 2.066 Å. The single-crystal XRD structure of UiO-66[33] indicates there are two distinct Zr–O bond lengths of 2.063 and 2.271 Å in the Zr cluster, though no specific assignment to $O^{2-}$ or $OH^{-}$ moieties was provided. Our DFT optimized Zr–O and Zr–OH bond lengths are consistent with the experimental observations and provide possible assignments for the two different bond lengths. These calculated bond lengths, paired with the non-zero experimental $\eta_Q$ value, indicate that the actual Zr rotational site symmetry is $\leq C_2$ rather than $C_4$. Despite the fractional occupancy of the O2 sites, our $^{91}$Zr NMR spectra and DFT calculations indicate there is a relatively ordered local short-range environment around Zr. It appears that one configuration is prevalent: two $OH^{-}$ groups are located at $O2^{i}$ and two $O^{2-}$ groups are at $O2^{ii}$.

The static $^{91}$Zr NMR spectrum of as-made UiO-66 containing water molecules in the pores (Fig. 1(b)) yielded a $C_Q(^{91}Zr)$ of 31.5(3) MHz, a $\eta_Q$ of 0.85(3) and a $\delta_{iso}$ of −100(50) ppm. The significant increase in $\eta_Q$ over activated UiO-66 corresponds to a lower degree of $^{91}$Zr EFG axial symmetry, which is due to guest water molecules in the pores. The water oxygen atom is situated 1.97 Å from the framework $OH^{-}$ group in the crystal structure (Fig. 1(c)).[33] Seeing as the primitive cell contains eight equivalent water positions, calculations of $^{91}$Zr NMR parameters following the plane-wave DFT geometry optimizations were performed on structures incorporating one to eight water molecules, with $C_Q$ and $\eta_Q$ results plotted in Fig. 1(c). It was found that $\eta_Q$ increased and $C_Q$ decreased with the number of water molecules, indicating a decrease of axial symmetry but an increase in overall spherical symmetry about Zr with increasing water population; this observation is in good agreement with the activated and as-made experimental findings. Cluster DFT calculations on the $\{Zr_8O_4(OH)_4(COO)_{12}(C_6H_4COOH)_{12}\cdot H_2O\}$ and $\{Zr_8O_4(OH)_4(COO)_{12}(C_6H_4COOH)_{12}\}$ models (Fig. S12(a), ESI†) yielded trends similar to those from plane-wave DFT calculations (Table 1). The case of UiO-66 demonstrates how $^{91}$Zr NMR is very sensitive to changes in the local environment owing to guest molecules, and how $^{91}$Zr NMR can be used to characterize the short-range order about Zr in MOFs; both approaches are significantly more effective when paired with DFT calculations.

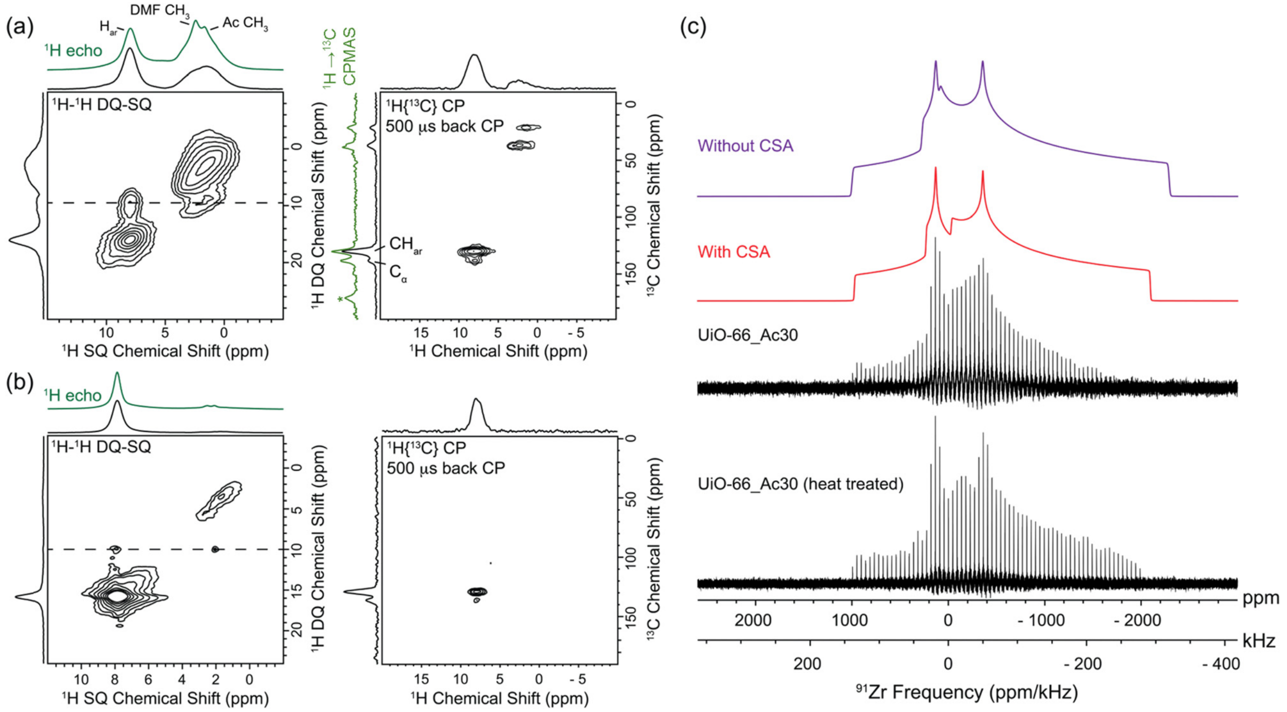

Fig. 2 (a) and (b) Fast MAS 2D $^1$H SQ-DQ (left) and 2D $^1$H{$^{13}$C} cross polarization heteronuclear correlation (right) NMR spectra of UiO-66 synthesized with acetic acid modulator (denoted UiO-66_Ac30) and the same sample of UiO-66 treated at 300 °C (labelled UiO-66_Ac30 (heat-treated)). The corresponding 1D $^1$H spin echo spectra are also shown (green traces). Spectra were acquired at a MAS frequency of 50 kHz and a magnetic field of 9.4 T. (c) Static and simulated static 35.2 T $^{91}$Zr NMR spectra of UiO-66_Ac30 and UiO-66_Ac30 (heat-treated). Analytical simulations of the $^{91}$Zr second-order quadrupole patterns are shown with CSA ($\delta_{iso}$ = −100 ppm, $\Omega$ = 200 ppm, $\kappa$ = 0.0, $C_Q$ = 32.5 MHz, $\eta$ = 0.79, $\alpha$ = 0, $\beta$ = 0, $\gamma$ = 0) and without CSA ($\delta_{iso}$ = −100 ppm, $C_Q$ = 34.5 MHz, $\eta$ = 0.79), where $\Omega$ and $\kappa$ are the span and skew of the CSA tensor and $\alpha$, $\beta$, and $\gamma$ are the Euler angles between the EFG and CS tensors.

Engineering linker or cluster defects in crystalline MOFs to better address applications in gas adsorption,[34] separation,[35] and catalysis is of significant interest.[36] While the impact of missing linker defects in UiO-66 has been studied in terms of structural and thermal stability, the local atomic-scale structure of these defects has been notoriously difficult to characterize.[37] A well-known study used single crystal XRD to determine that missing linker structural defects originated from water molecules coordinated directly to the zirconium centers, with charge compensation provided by a hydroxide ion that was hydrogen-bonded to a nodal $\mu_3$-OH species.[33] Despite several efforts, a definitive determination of the local structure of these UiO-66 defects has remained elusive.

To further investigate the impact of missing linker defects, UiO-66 synthesized with an acetic acid modulator to increase the concentration of defects (termed UiO-66_Ac30) and a sample of UiO-66_Ac30 treated at 300 °C to remove acetate groups (denoted UiO-66_Ac30 (heat-treated)) were examined using solid-state NMR spectroscopy. The amount of acetic groups in UiO-66_Ac30 was estimated to be 12% from $^1$H solution NMR spectra (Fig. S13, ESI†). The one-dimensional $^1$H and $^{13}$C NMR spectra of UiO-66_Ac30 (Fig. 2(a)) contain signals originating from the acetate, DMF and phenyl groups.[38] The resonance assignments were confirmed from the through-space correlations evident in $^1$H–$^{13}$C CP HETCOR NMR spectra (Fig. 2(a), right). The two-dimensional $^1$H–$^1$H DQ-SQ NMR spectrum (Fig. 2(a), left) reveals that the DMF methyl groups and acetate moieties are spatially proximate to aromatic hydrogen atoms. These observations are indicative of interactions between solvent DMF and the UiO-66 carboxylate framework linkers. Note that the secondary $^1$H NMR signal from DMF, typically found between 7 and 8 ppm, is not prominently visible in our $^1$H MAS NMR spectra of the as-made UiO-66 samples due to the strong intensity of the nearby aromatic signal. This observation aligns with previous studies on UiO-66 MOFs that reported the secondary DMF signal was present as only a weak resonance or a minor shoulder feature in the spectra.[23,38,39]

Heat treatment of UiO-66_Ac30 to produce UiO-66_Ac30 (heat-treated) resulted in several spectral changes (Fig. 2(b)). The $^1$H signal intensity of the methyl groups in UiO-66_Ac30 (heat-treated) was significantly diminished. The $^1$H NMR signals at 2.1 ppm and 2.5 ppm from UiO-66_Ac30 likely originate from terminal $\mu_1$-OH and/or $\mu_1$-OH$_2$ groups at defect sites,[39] but may also have contributions from $\mu_3$-OH species in regions without defects.[38,40–42] After heat treatment of UiO-66_Ac30, the aromatic and C$_\alpha$ $^{13}$C NMR signals were shifted from 130 ppm to 129 ppm and 138 ppm to 136 ppm, respectively, which was presumably due to the removal of DMF. As the samples were exposed to air after synthesis, the removal of UiO-66_Ac30 (heat-treated) acetate groups likely resulted in the formation of $\mu_1$-OH or $\mu_1$-OH$_2$ species at the vacant Zr sites in the cluster.

To probe the Zr local environment further, $^{91}$Zr solid-state NMR experiments were performed at 35.2 T. The $^{91}$Zr NMR spectrum of UiO-66_Ac30 contains a well-defined second-order quadrupolar powder pattern that has features which can only be modeled using $^{91}$Zr CSA (Fig. 2(c)). The similarity in the measured quadrupolar parameters between UiO-66_Ac30 and UiO-66 (as-made), along with the well-defined features of the $^{91}$Zr NMR spectrum of UiO-66_Ac30, indicates the first coordination sphere of Zr is largely preserved in UiO-66_Ac30 and contains both BDC and acetate ligands. $^{91}$Zr QCPMG experiments on UiO-66_Ac30 (heat-treated) revealed that a longer $T_2'(^{91}\mathrm{Zr})$ was present, resulting in a slower decay of the signal during the QCPMG echo train, which in turn yielded a higher signal-to-noise ratio. This observation was somewhat unexpected in these non-decoupled spectra, since the presence of $\mu_1$-OH hydrogen proximate to $^{91}$Zr should result in stronger $^{91}$Zr–$^1$H dipolar couplings and a reduced $T_2'$. The observed $^{91}$Zr NMR spectrum of UiO-66_Ac30 (heat-treated) appears otherwise identical to that of UiO-66_Ac30. This could be because the relatively small amount of defective Zr sites are associated with much higher $C_Q(^{91}\mathrm{Zr})$ values, making the corresponding very broad resonances nearly impossible to observe using $^{91}$Zr solid-state NMR experiments.

We performed DFT calculations on cluster models to generate potential models for defective Zr sites in UiO-66 (Fig. S12, ESI†). The defective unsaturated Zr$^{4+}$ center yielded a calculated $C_Q$ value of 69.6 MHz, which would give rise to resonances four times broader than those of the main $^{91}$Zr NMR signals, making them challenging or impossible to observe using existing NMR instrumentation and methods. When OH$^-$ or H$_2$O is bound to a defective Zr$^{4+}$ center at distances larger than *ca.* 3 Å, the calculated $C_Q$ also becomes very large (*i.e.*, $>50$ MHz, Fig. S12(b), ESI†). When the bond length between Zr and $\mu_1$-OH at defect sites in UiO-66 is relatively short (*e.g.*, 2.26 Å, similar to that of Zr-$\mu_3$-OH), DFT calculations predict a comparable $C_Q(^{91}\mathrm{Zr})$ value to that of defect-free Zr in UiO-66; distinguishing between the two different signals does not appear to be possible from these $^{91}$Zr NMR experiments. This explanation aligns with the structural similarity proposed in the Cluster 4 model (Fig. S12, ESI†), where the local Zr environment containing defects could be nearly identical to that of defect-free Zr. This is consistent with the hypothesis of $\mu_1$-OH or $\mu_1$-OH$_2$ species formation at the vacant Zr sites in the cluster. While these results indicate that $^{91}$Zr solid-state NMR could potentially be used to probe the local environment in defective Zr MOFs, measures to significantly increase experimental sensitivity and resolution would be required. Further evaluation will be necessary to unequivocally establish the local structure of these defects in UiO-66, which is beyond the scope of this work.

The concept of reticular synthesis, in which MOFs of similar topology can be created using related organic linkers (*e.g.*, linkers of different lengths), is instrumental to the design and synthesis of new MOFs.[43,44] A striking example of reticular synthesis is modification of the UiO-66 synthesis to generate UiO-67; the linker was changed from BDC to 4,4′-biphenyldicarboxylate (BPDC), resulting in a pore size increase from 8 Å to 12 Å, while the Zr$_6$O$_8$(OH)$_8$ SBU and overall MOF topology were preserved.[32] The static $^{91}$Zr NMR spectrum of UiO-67 at 35.2 T (Fig. 3(b)) features a single Zr site corresponding to a $C_Q(^{91}\mathrm{Zr})$ of 23.2(7) MHz, a $\eta_Q$ of 0.91(3) and a $\delta_{\mathrm{iso}}$ of −20(30) ppm, which has lower $C_Q$ and higher $\eta_Q$ values than

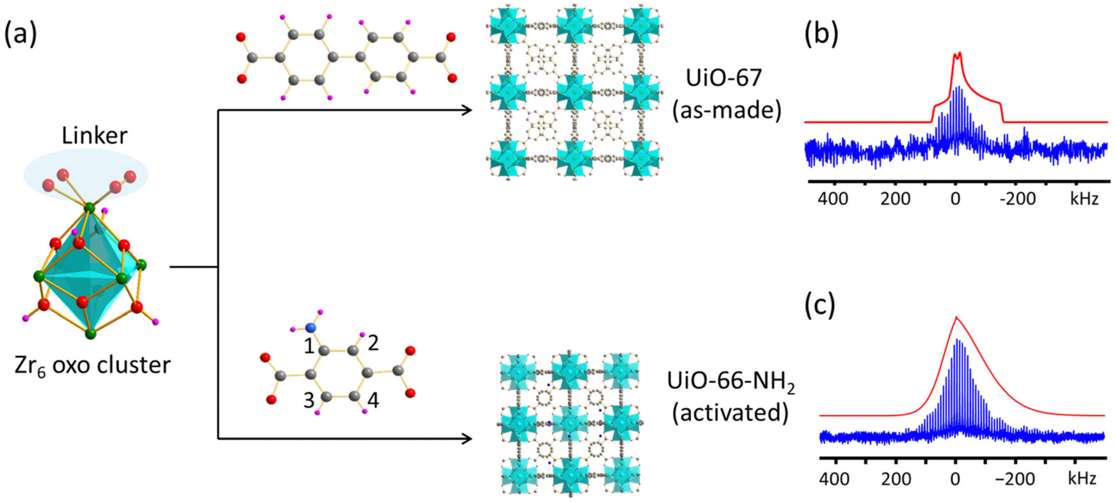

Fig. 3 The short- and long-range structure of UiO-67 and UiO-66-NH$_2$ are shown in (a), along with their respective organic linkers. The experimental (blue) and simulated (red) static $^{91}$Zr NMR spectra of UiO-67 and UiO-66-NH$_2$ at 35.2 T are given in (b) and (c), respectively.

those observed from UiO-66. Potential root causes for the different NMR parameters between UiO-66 and -67 were then investigated.

The local geometry and symmetry at Zr is intimately linked to $^{91}$Zr EFG parameters, particularly $C_Q(^{91}Zr)$. In an Archimedean antiprism with eight local nodes (*i.e.*, the coordination environment about Zr in this system), the $s/l$ ratio can be used to quantify the degree of local distortion from ideal geometry, where $s$ refers to the edge length of the square planes and $l$ is the edge length of triangular faces in the distorted antiprism (Fig. S14(b), ESI†). The distortion parameter $\xi$, also known as the Poraï-Koshits and Aslanov criteria,[26,45] can then be used to measure distortion. In this case, $\xi = \sum|s_i/l_i - s_0/l_0|$; a perfect antiprism yields $\xi = 0$, where larger $\xi$ values correspond to higher degrees of distortion and thus increased $C_Q(^{91}Zr)$. An examination of geometry-optimized structures reveals the Zr local distortion parameter in UiO-67 ($\xi = 1.11$) is smaller than that of UiO-66 ($\xi = 1.33$), which explains the lower $C_Q(^{91}Zr)$ value observed in UiO-67. The relatively larger $\eta_Q$ and lower axial symmetry at Zr in UiO-67 may originate from the flexibility of BPDC linker phenyl rings.[46] To further investigate, DFT calculations were performed on two cluster models of $\{Zr_8O_4(OH)_4(COO)_{12}(C_{12}H_8COOH)_{12}\}$ (Fig. S14, ESI†), where the first model (model 1) employed two coplanar phenyl rings, while the second model (model 2) introduced a dihedral angle of 32.7° between the two phenyl groups, which was taken from the SCXRD structure.[46] DFT calculations predicted a relatively smaller $C_Q$ value and a larger $\eta_Q$ when the non-zero dihedral angle was present, with calculations producing values similar to experimental findings. In this instance, the combination of $^{91}$Zr NMR experiments and DFT calculations illustrates how $^{91}$Zr NMR parameters are sensitive not only to the local bonding geometry, but also to linkers and their orientations beyond the immediate coordination environment.

Derivatives of UiO-66 can be prepared by introducing functional groups, such as –NH$_2$, to address specific applications. For instance, the CO$_2$/N$_2$ selectivity of UiO-66-NH$_2$ is enhanced over that of UiO-66, owing to strong interactions between CO$_2$ and the –NH$_2$ linker group.[47] The various possible crystallographic positions of the –NH$_2$ group introduces significant uncertainty to the UiO-66-NH$_2$ unit cell. The PXRD patterns of UiO-66-NH$_2$ and UiO-66 are almost identical, indicating commonalities between long-range structures (Fig. S1, ESI†). The $^1$H–$^{13}$C CP/MAS NMR and $^1$H MAS NMR (Fig. S4, ESI†) of activated UiO-66-NH$_2$ indicates that there are very few guest solvent molecules remaining after activation. The $^1$H–$^{13}$C CP/MAS NMR spectra of UiO-66-NH$_2$ feature relatively broader signals compared to the corresponding spectra of UiO-66, which is due to the presence of increased local disorder (Fig. S4, caption, ESI†).[40] The $^{91}$Zr NMR experiments at 35.2 T were performed on an activated sample to prevent any influence on the local environment from guest solvents. The static $^{91}$Zr NMR spectrum of UiO-66-NH$_2$(activated) at 35.2 T (Fig. 3(c)) features a broad, asymmetric powder pattern that lacks clear features and tails off in intensity toward the low frequency range; these signs are indicative of a distribution of EFG parameters arising from local disorder.

The $^{91}$Zr NMR lineshape of UiO-66-NH$_2$ is featureless, arising from a Gaussian-like distribution of $^{91}$Zr NMR parameters. This stands in marked contrast to the $^{91}$Zr NMR spectra of both as-made and activated UiO-66 (Fig. 1), which exhibit well-defined lineshapes typical of a quadrupolar nucleus in an ordered local environment. As the Zr$_6$-oxo cluster in the UiO-66 and UiO-66-NH$_2$ materials is the same, the differences between the $^{91}$Zr NMR spectra of UiO-66-NH$_2$ and UiO-66 must originate from the –NH$_2$ group of the organic linker in UiO-66-NH$_2$. The linker appears to be associated with local disorder about Zr beyond the first coordination sphere.

The EFG at Zr in a given system is determined by both (i) the immediate local environment and (ii) the surroundings beyond the first coordination sphere. In situations of high local order about Zr, the $^{91}$Zr EFG tensor and NMR spectrum correspond to well-defined $C_Q$ and $\eta_Q$ values. In contrast, when local disorder is present about Zr, there is an intrinsic distribution of $^{91}$Zr EFG tensor parameters arising from the range of potential local chemical environments. An extended Czjzek model (ECM) can be used to quantify the effects of local disorder on the $^{91}$Zr EFG distribution.[48] The ECM is appropriate for modeling the EFG distribution in a local Zr environment that contains contributions from both the ordered immediate coordination environment and the disordered, more distant surroundings. An ECM utilizes a combination of fixed $C_Q$ and $\eta_Q$ values along with a separate distribution of values drawn from a range of $C_Q$ and $\eta_Q$; a more detailed description on ECM is contained in the ESI.† An ECM allows for a quantitative measure of the local disorder in MOFs based on NMR spectra.[15,49]

In the case of UiO-66-NH$_2$, an ECM using a fixed $C_Q$($^{91}$Zr) of 26.5(8) MHz and fixed $\eta_Q$ of 0.72(5) was used to fit the experimental $^{91}$Zr NMR spectrum, along with a 0.6 measure of disorder ($\epsilon$); simulations using other $\epsilon$ values are shown in Fig. S15(a) (ESI†) and the best-fit $C_Q$ and $\eta_Q$ distributions are illustrated in Fig. S15(b) (ESI†). The fixed $^{91}$Zr EFG contribution to the NMR spectrum of UiO-66-NH$_2$ arises from the ordered ZrO$_8$ immediate local environment, which is similar to that of UiO-66. The need for an ECM and large distribution in $^{91}$Zr NMR parameters (*i.e.*, $\epsilon = 0.6$) is rooted in the disordered nature of the amino linker groups, since a given linker amino group may assume one of four positions with respect to Zr. One Zr$_6$ cluster (Zr$_6$O$_8$(OH)$_8$(BDC-NH$_2$)$_{12}$) in the primitive cell is attached to twelve linkers, which leads to $4^{12} \approx 1.6 \times 10^7$ different spatial atomic configurations beyond the first coordination sphere of Zr, and a correspondingly sizable distribution of $^{91}$Zr EFG parameters. DFT calculations of $^{91}$Zr NMR parameters using the reported most stable configuration of UiO-66-NH$_2$ based on relative energies[50] yielded $C_Q$ and $\eta_Q$ values close to the fixed experimental $C_Q$ and $\eta_Q$ used in the ECM simulations (Table 1), confirming that the immediate local environment about Zr is relatively ordered; however, $^{91}$Zr NMR simulations based on DFT calculations were unsatisfactory matches for the entire experimental spectrum (Fig. S16, ESI†), owing to local disorder beyond the first coordination sphere of Zr. These UiO-66-NH$_2$ results clearly show how $^{91}$Zr NMR can be used to investigate local disorder in MOFs and to confirm the presence of a distribution of Zr local environments.

MOF-808 is a mesoporous MOF with high thermal and mechanical stability that has potential applications in gas separation, gas adsorption, and catalysis.[51] The MOF-808 framework is composed of Zr$_6$O$_4$(OH)$_4$ nodes connected by benzene-1,3,5-tricarboxylate (BTC) linkers to form a structure with one unique Zr site that crystallizes in the $Fd\bar{3}m$ cubic space group (Fig. 4(a)). Each Zr$_6$ node has twelve-fold connectivity and is bound to six BTC linkers and six formate ligands. The $^{91}$Zr NMR spectra of MOF-808 at 19.6 T (Fig. 4(b)) can be simulated by a single Zr resonance corresponding to a $C_Q$ value of 18.4(5) MHz and a $\eta_Q$ of 0.90(3). The relatively lower $C_Q$ and higher $\eta_Q$ values *versus* the UiO-66/67 MOFs are due to the different Zr local coordination modes. In MOF-808, each Zr is bound to four $\mu_3$-O atoms, two carboxyl O atoms, and two O atoms from terminal formate ions, while Zr is bound to four $\mu_3$-O atoms and four carboxyl O atoms in UiO-66/67. To investigate the impact of these different local configurations, both plane-wave and cluster DFT calculations were performed on the optimized structure, yielding results in good agreement with experimental findings (Table 1).

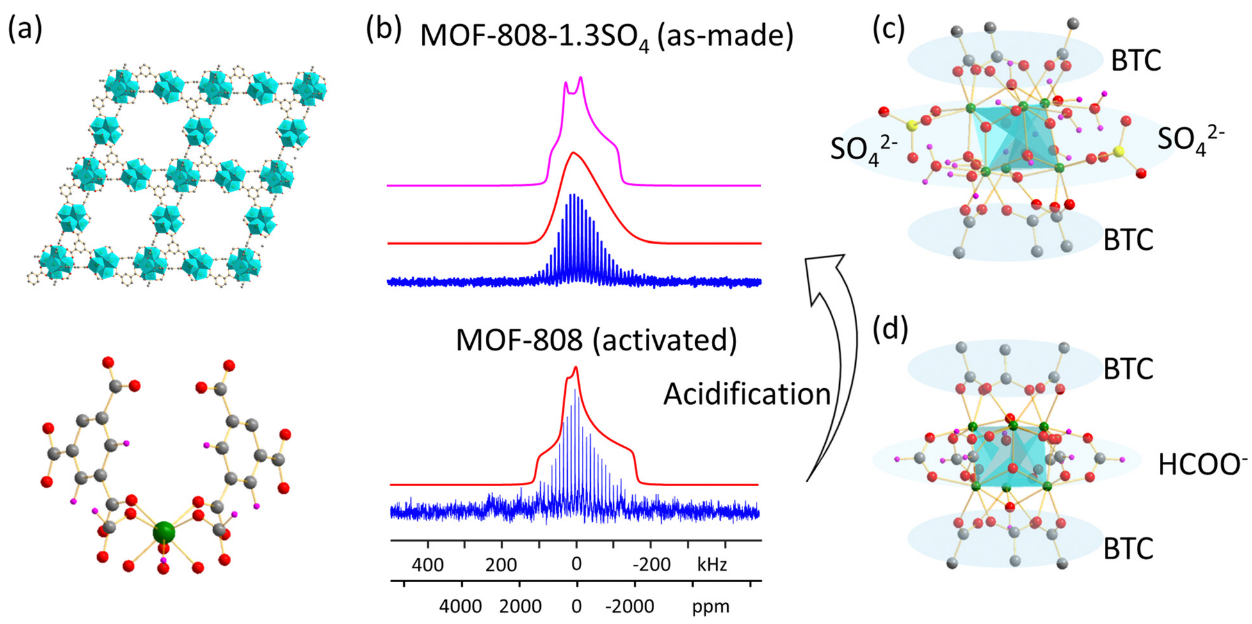

Fig. 4 (a) The long-range structure of MOF-808 (top) and local environment about Zr (bottom); (b) experimental (blue) and simulated (red, ECM) static $^{91}$Zr NMR spectra of activated MOF-808 at bottom, with experimental (blue) and simulated (red is ECM, purple is single-site simulation) static $^{91}$Zr NMR spectra of MOF-808-1.3SO$_4$ at 19.6 T found at top. (c) The Zr$_6$ oxo cluster with two HCOO$^-$ substituted by SO$_4^{2-}$, and (d) the Zr$_6$ oxo cluster in pristine MOF-808.

A sulfated version of MOF-808 was synthesized using post-synthetic modification[52] of activated MOF-808 with 0.01 M sulfuric acid for 24 hours, yielding MOF-808-1.3$SO_4$. The product was analogous to MOF-808-$x$$SO_4$, where $x$ is the average number of sulfate groups per secondary building unit (SBU) from elemental analysis;[53] an illustration of a $Zr_6$ oxo cluster substituted with two $SO_4^{2-}$ groups is shown in Fig. 4(c). The $^1H$–$^{13}C$ CP/MAS NMR spectrum of MOF-808-1.3$SO_4$ contains a much less intense carboxylic carbon signal compared to that of MOF-808 (Fig. S6, ESI†), which indicates that $HCOO^-$ groups have been partially replaced by $SO_4^{2-}$. In this system, the $SO_4^{2-}$ ions replace formate ions and directly form Zr–O bonds.[52] The $^{91}Zr$ NMR spectra of MOF-808-1.3$SO_4$ is shown in Fig. 4(b), along with our attempts to use simulations involving both a discrete set of NMR parameters and an ECM to extract $^{91}Zr$ NMR parameters. The $^{91}Zr$ NMR spectrum of acidified MOF-808-1.3$SO_4$ is relatively featureless, in contrast to the more well-defined spectrum of activated MOF-808. These results indicate there is some degree of local disorder about Zr centers in the acidified MOF, which is due to the random replacement of formate ions with $SO_4^{2-}$ groups. The $^{91}Zr$ NMR powder pattern of MOF-808-1.3$SO_4$ was successfully simulated using an ECM employing a fixed $C_Q(^{91}Zr)$ value of 17.0(5) MHz, a fixed $\eta_Q$ of 0.72(4), and a 0.35 measure of disorder ($\epsilon$) (Fig. S17, ESI†). The fixed $^{91}Zr$ EFG tensor components originate from the coordinated $\mu_3$-O atoms and O atoms from BTC linkers, while the disordered component (*i.e.*, $\epsilon$) arise from the various possible partial substitution configurations of the six proximate formate ligands by $SO_4^{2-}$ ions. The $\epsilon$ value in the $^{91}Zr$ ECM NMR simulation of MOF-808-1.3$SO_4$ is substantially smaller than that of UiO-66-$NH_2$, since there are far fewer possible local environments. A more intense acidification treatment using 0.1 M $H_2SO_4$ was applied to obtain MOF-808-2.3$SO_4$, which yielded a $^{91}Zr$ NMR spectrum very similar to that of MOF-808-1.3$SO_4$, and no significant differences were apparent with regards to local order (Fig. S18(a), ESI†). In contrast, the $^{91}Zr$ NMR signals in the time domain (*i.e.*, prior to Fourier transform) were clearly distinct, with the MOF-808-2.3$SO_4$ signal associated with a $T_2'$ relaxation time *ca.* 25% less than that of the MOF-808-1.3$SO_4$ version (Fig. S18(b), ESI†). This finding suggests that while there may be a limit to the level of acid substitution level in this system quantifiable by $^{91}Zr$ NMR frequency domain spectra, the time domain signals can still yield valuable information on the local Zr environment. These examples illustrate how $^{91}Zr$ NMR can be used to understand the degree of local order about metal centers in MOFs.

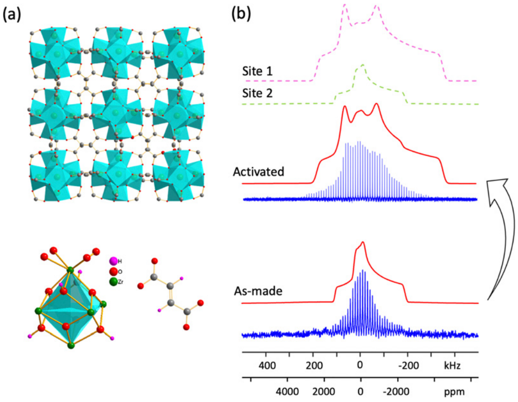

Fig. 5 (a) The long-range structure of MOF-801 (top) and local environments about Zr and the fumaric acid linker; (b) experimental (blue) and simulated (red) static $^{91}Zr$ NMR spectra of as-made and activated MOF-801 at 19.6 T, where an ECM was used to simulate the as-made MOF-801 spectrum.

The intrinsically high stability of Zr-based MOFs makes these materials excellent candidates for water capture. MOF-801, or Zr-fumarate ($Zr_6O_4(OH)_4(fumarate)_6$), has one of the highest documented MOF water uptake values, does not lose water capacity after five adsorption and desorption cycles, can be readily regenerated at room temperature,[51] and also has a high adsorption capacity for hydrocarbons.[54] The structure of MOF-801 was solved using PXRD[55] and SCXRD.[51] MOF-801 has one unique Zr site and resides in the cubic $Pn\bar{3}$ space group, which is of lower symmetry than UiO-66; no face-centered symmetry is present, owing to the fumarate linker that is not strictly linear (Fig. 5(a)). The static $^{91}Zr$ NMR spectrum of as-made MOF-801 at 19.6 T is shown in Fig. 5(b), featuring spectral intensity that gradually tails off to low frequency, indicating that some degree of disorder is present; the spectrum was accordingly simulated using an ECM (Table 1). The $^{91}Zr$ NMR parameters of as-made MOF-801 indicate that a significantly higher degree of overall symmetry about Zr (lower $C_Q$) but a slightly lower amount of axial symmetry (higher $\eta_Q$) are present in comparison to Zr within UiO-66. The presence of a hydrogen-bonded network of water molecules in the as-made MOF-801 pores explains both $^{91}Zr$ NMR trends,[51] and is one source of the local disorder at Zr.

Thermal activation was performed to remove water from the pores of MOF-801. The $^{91}Zr$ NMR spectrum of activated MOF-801 again consisted of a distribution of similar Zr sites. This spectrum was simulated using a dominant signal of 85% relative intensity with a $C_Q$ of 29.0(10) MHz and $\eta_Q$ of 0.65(5), along with a minor resonance of 15% intensity using the same $^{91}Zr$ NMR parameters of as-made MOF-801; the minor site arises from insufficient activation or water adsorption from air during NMR sample preparation. Plane-wave DFT calculations on the fully optimized empty (*i.e.*, activated) structure of MOF-801 yielded a $C_Q$ of 30.2 MHz and $\eta_Q$ of 0.62, which were very good matches to the major Zr signal in the activated NMR spectrum. To probe the effect of adsorbed water molecules on the $^{91}Zr$ NMR parameters, cluster DFT calculations were performed (Fig. S19, ESI†). The $\{Zr_8O_4(OH)_4(COO)_{12}(C_2H_2COOH)_{12}\cdot 4H_2O\}$ model using the water position closest to Zr based on the crystal structure[51] produced a relatively smaller $C_Q$ of 26.6 MHz but a larger $\eta_Q$ of 0.84, and both values were closer to the as-made MOF-801 experimental values. In contrast, cluster DFT calculations on $\{Zr_8O_4(OH)_4(COO)_{12}(C_2H_2COOH)_{12}\}$ without water yielded a larger $C_Q$ of 31.2 MHz and smaller $\eta_Q$ of 0.50, which were better matches to the activated MOF-801 experimental data. These $^{91}Zr$ NMR and DFT calculation results illustrate how $^{91}Zr$ NMR parameters are highly sensitive to changes in the local environment.

The selection of a specific modulator during MOF synthesis is very important, as this can affect MOF nucleation, topology, and properties. The reaction of $ZrCl_4$ and 2,5-thiophenedicarboxylic acid ($H_2TDC$) in DMF (DMF = dimethylformamide), using 180 equivalents of acetic acid as the modulator, yields the $Zr_6O_6(OH)_2(TDC)_{4.5}(CH_3COO)$ MOF, also known as DUT-68(Zr), which resides in the $Im3\bar{m}$ space group.[56] The $^{91}$Zr NMR spectrum at 19.6 T (Fig. 6(c)) indicates that a distribution of Zr local environments are present; simulations using a Czjzek model yielded $\sqrt{\langle C_Q{}^2 \rangle} = 14.9$ MHz (Fig. S20, ESI†). Further examination of the SCXRD structure[56] revealed two potential sources for the $^{91}$Zr NMR parameter distribution (Fig. S21, ESI†): (i) the framework features two crystallographically independent eight-connected $Zr_6O_6(OH)_2(TDC)_{4.5}(CH_3COO)$ clusters, along with six inequivalent Zr sites in each Zr-oxo SBU; (ii) DUT-68 has four relatively large pores measuring 27.7 Å, 13.9 Å, 12.5 Å and 8 Å in diameter, which contain occluded and disordered Zr-oxo clusters.[56] The multitude of Zr local environments resulting from these two structural factors give rise to significant local disorder, explaining the relatively featureless $^{91}$Zr NMR spectral appearance.

DUT-69(Zr) can be obtained from the same route as DUT-68(Zr), but using only 50 equivalents of the acetic acid modulator during synthesis. DUT-69(Zr) has a composition of $Zr_6O_4(OH)_4(TDC)_5(CH_3COO)_2(H_2O)_2$ and consists of a uninodal 10-connected framework with the *bct* topology, along with octahedral cages measuring *ca.* 5 Å in diameter (Fig. 6(b)). There is a single type of $Zr_6$ cluster in DUT-69 that features six inequivalent Zr sites, with the local SBU connectivity shown in Fig. S22(a) (ESI†). In the SBU, Zr1 and Zr4 are each bound to three TDC linkers and one water, Zr2 and Zr5 are connected to three TDC linkers and one molecule of $CH_3COO^-$, while Zr3 and Zr6 are coordinated to four TDC linkers. The static $^{91}$Zr NMR spectrum of DUT-69 at 19.6 T is shown in Fig. 6(c). Accurate simulation required the use of two distinct Zr signals arising from two unique Zr sites (Table 1); site 1 corresponded to a $C_Q$ of 18.5(3) MHz and $\eta_Q$ of 0.38(2), and site 2 was simulated using a $C_Q$ of 19.1(4) MHz and $\eta_Q$ of 0.85(3). Both plane-wave and cluster DFT calculations were performed on the optimized structure (Table S4, ESI†) to assign the two $^{91}$Zr NMR resonances. Simulated NMR spectra based on the DFT-calculated $^{91}$Zr NMR parameters were constructed (Fig. S22, ESI†), which contained lineshapes similar to the experimental spectrum. These simulated spectra were used as guides to assign the experimental $^{91}$Zr NMR spectrum; site 1 in the experimental spectrum was assigned to Zr2 and Zr3, while site 2 was assigned to Zr1, Zr4, Zr5, and Zr6. We note that both plane-wave and cluster DFT approaches overestimated experimental $C_Q$ values, which is likely due to inaccuracies regarding the $CH_3COO^-$ local environment in the crystal structure.[56]

During the review of our manuscript, a study by Nadol *et al.*[23] was published, employing low-temperature (140 K) $^{91}$Zr NMR with the WURST-CPMG sequence to investigate the stability of Zr MOFs, including UiO-66 and MOF-801. Their work focused on analyzing Zr MOF stability, while our study explores local disorder across 11 Zr MOFs. Significant differences in $^{91}$Zr NMR parameters were observed, likely due to temperature effects. For UiO-66, Nadol *et al.* reported $\delta_{iso} = -28 \pm 50$ ppm, $C_Q = 22.1$ MHz, and $\eta_Q = 0.61$ at 140 K, while our room-temperature results yielded $\delta_{iso} = -100 \pm 50$ ppm, $C_Q = 31.5 \pm 0.3$ MHz, and $\eta_Q = 0.85 \pm 0.03$. Similarly, for MOF-801, their parameters at 140 K were $\delta_{iso} = -30$ ppm, $C_Q = 31.8$ MHz, and $\eta_Q = 0.75$, compared to our values of $\delta_{iso} = 0 \pm 40$ ppm, $C_Q = 29.0 \pm 1.0$ MHz, and $\eta_Q = 0.65 \pm 0.03$ at 298 K.

While Nadol *et al.* enhanced the signal-to-noise ratio by performing experiments at 140 K, our use of a 35.2 T ultra-high magnetic field with a standard CPMG sequence establishes that

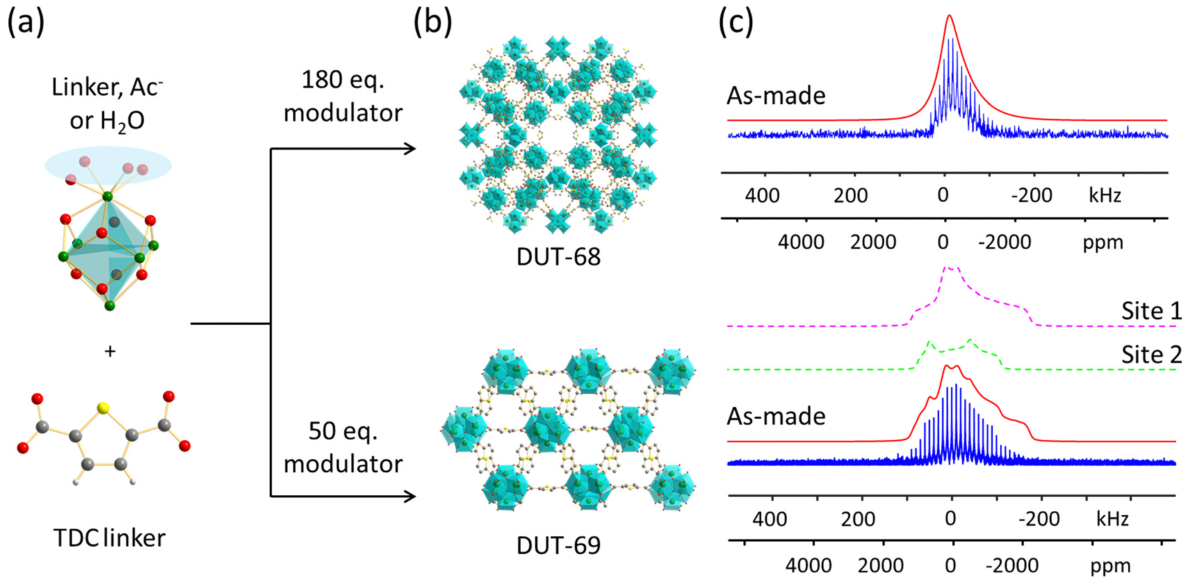

Fig. 6 (a) The secondary building unit and organic TDC linker of DUT-68 and DUT-69 are shown, along with (b) the long-range structures of DUT-68 and DUT-69. In (c), the experimental (blue) and simulated (red) static $^{91}$Zr NMR spectra of DUT-68 at 19.6 T are depicted at top, and at bottom, the experimental (blue) and simulated (red sum, purple and green individual sites) static $^{91}$Zr NMR spectra of DUT-69 at 19.6 T are provided.

high signal-to-noise ratio $^{91}$Zr spectra can be achieved at room temperature. Performing experiments at ultrahigh field allows researchers to probe the temperature-dependent chemical environments of Zr sites under conditions closer to those envisoned for practical applications.

## Conclusions

In summary, wideline and ultra-wideline $^{91}$Zr solid-state NMR spectra of Zr MOFs have been successfully obtained, yielding rich information on the Zr local environments and local order in each system. The $^{91}$Zr solid-state NMR spectra are sensitive to the nature of coordinated ligands along with the degree of local disorder, and indicate the presence of guest solvents, specific linker orientations, and the number of possible linker configurations; these experiments can also shed light on the results of ion exchange reactions. Plane-wave and cluster DFT calculations are valuable complementary methods that can assist in the analysis of $^{91}$Zr NMR parameters and their specific structural origins. The detailed data available from $^{91}$Zr SSMR spectroscopy and DFT calculations in this work illustrates how this approach should be a powerful avenue to investigate Zr-containing MOFs going forward.

## Experimental details

### Sample synthesis

All chemicals were purchased from Sigma-Aldrich and used without further purification.

**UiO-66**[32]. A mixture of $ZrCl_4$ (0.265 g, 1.135 mmol) and 1,4-benzenedicarboxylic acid ($H_2BDC$) (0.170 g, 1.135 mmol) was dissolved in 30 mL of dimethylformamide (DMF). The mixture was then sealed in a Teflon-lined autoclave and placed in an oven set at 120 °C for 24 h. The resulting white solid was isolated *via* centrifugation and then washed thoroughly with DMF and ethanol. The powder was solvent exchanged with acetone and dried in an oven set to 80 °C, yielding UiO-66(as-made) powder product. The UiO-66(as-made) powder was then evacuated at 150 °C under dynamic vacuum (<1 mbar) for 24 hours to yield UiO-66(activated) powder.

**UiO-66_Ac30**[57]. A mixture of $ZrCl_4$ (0.265 g, 1.135 mmol), $H_2BDC$ (0.170 g, 1.135 mmol) and acetic acid (HAc) (30 mmol) was dissolved in 30 mL of dimethylformamide (DMF). The mixture was then sealed in a Teflon-lined autoclave and placed in an oven set at 120 °C for 24 h. The resulting white solid was isolated *via* centrifugation and then washed thoroughly with DMF and ethanol. The powder was dried in an oven set at 80 °C, yielding a UiO-66_Ac30 product. The resulting UiO-66_Ac30 was then evacuated at 300 °C under dynamic vacuum (<1 mbar) for 24 hours to yield UiO-66_Ac30 (heat-treated).[57]

**UiO-66-NH$_2$**[32]. The synthesis was performed analogous to that of UiO-66, but by replacing the $H_2BDC$ precursor with same equivalent moles (0.206 g, 1.135 mmol) of 2-aminoterephthalic acid ($H_2BDC$-$NH_2$). The activation procedure was the same as that performed for UiO-66.

**UiO-67**[32]. The synthesis was carried out in the same manner as for UiO-66, but with a substitution of the $H_2BDC$ reagent with the same equivalent moles (0.275 g, 1.135 mmol) of biphenyl-4,4-dicarboxylic acid ($H_2BPDC$).

**MOF-801**[51]. Both the $ZrOCl_2 \cdot 8H_2O$ (0.320 g, 1.0 mmol) and fumaric acid (0.12 g, 1.0 mmol) reagents were dissolved in a solution of 4 mL DMF and 1.4 mL formic acid, following which the mixture was placed into a sealed Teflon-lined autoclave and heated in an oven at 130 °C for 6 h. After cooling to room temperature, the mixture was filtered, and the isolated solid was then washed with DMF and methanol three times and dried in an oven at 80 °C. The product was denoted as MOF-801 (as-made). The as-made MOF-801 powder was then evacuated at 150 °C under dynamic vacuum (<1 mbar) for 24 hours to yield activated MOF-801.

**MOF-808**[51]. $ZrOCl_2 \cdot 8H_2O$ (0.97 g, 3.0 mmol) and trimesic acid ($H_3BTC$, 0.21 g, 1.0 mmol) were first dissolved in 45 mL of DMF and 45 mL of formic acid. The resulting mixture was then placed in a sealed screw-capped glass jar, which was heated at 130 °C in an oven for two days. The resulting white precipitate was collected by filtration and washed three times with 200 mL of DMF. The product was then dried in an oven set at 80 °C, yielding MOF-808(as-made). The MOF-808(as-made) powder product was evacuated at 150 °C under dynamic vacuum (<1 mbar) for 24 hours to yield MOF-808 (activated).

**MOF-808-1.3SO$_4$**[52]. MOF-808 (as-made) was activated under dynamic vacuum (<1 mbar) at 150 °C for 24 h. The resulting activated powder (0.50 g, 0.37 mmol) was then immersed in 50 mL of 0.01 M sulfuric acid (0.5 mmol) for 24 h; during acid immersion, the mixture was stirred once approximately every two hours. The powdered product was then filtered and washed with water, acetone and chloroform. The resulting MOF-808-1.3$SO_4$ product was dried under vacuum at room temperature.

**MOF-808-2.3SO$_4$**[52]. An identical procedure as that for MOF-808-1.3SO4 was followed, with the exception that 50 mL of 0.05 M sulfuric acid was used.

**DUT-68**[56]. 230 mg (1 mmol) of $ZrCl_4$ was dissolved in 25 mL of DMF and subjected to sonication for 10 min. To this mixture, 258 mg (1.5 mmol) of 2,5-thiophenedicarboxylic acid ($H_2TDC$) was added; sonication was then performed for 5 min, after which 11 mL or 183 mmol of acetic acid was added. The mixture was then sonicated for another 10 min, transferred to a sealed screw-capped glass jar, and heated in an oven at 120 °C for 72 h. The product was obtained as a powder, which was dried under vacuum at room temperature.

**DUT-69**[56]. $ZrCl_4$ (230 mg, 1 mmol) was dissolved in DMF (50 mL) *via* sonication for 10 min, following which $H_2TDC$ (172 mg, 1 mmol) was added to the solution and the resulting mixture was sonicated for 5 min. In this case, 3 mL or 50 mmol of acetic acid was then added to the mixture and sonicated for 10 min. The solution was then placed in a sealed screw-capped glass jar and heated in an oven at 120 °C for 12 h. The powdered product was dried under vacuum at room temperature.

Different activation procedures were used to ensure complete removal of guest molecules while preserving framework structure. For most MOFs examined aside from UiO-66_Ac30, activation at 150 °C under dynamic vacuum (<1 mbar) for 24 hours was used to remove non-coordinated solvent molecules. For UiO-66_Ac30, a higher activation temperature of 300 °C under vacuum was required to effectively eliminate $CH_3COOH$, $H_2O$, and DMF molecules directly coordinated to the Zr centers based on the procedure described by Kandiah *et al.*[53]

### Solid-state NMR experiments

All $^{91}$Zr solid-state NMR experiments at 35.2 T ($\nu_0(^{91}\mathrm{Zr})$ = 139.46 MHz) were performed on the series-connected hybrid (SCH) magnet[58] at the National High Magnetic Field Laboratory (NHMFL) in Tallahassee, FL, USA, using a Bruker NEO console. A single channel home-built static probe with a 4 mm coil was used for static quadrupolar Carr–Purcell–Meiboom–Gill (QCPMG)[30] NMR experiments with a 90° pulse length of 1.45 μs. The post-pulse ring-down time in the Meiboom–Gill (MG) loops was set to 20.3 μs, and the number of MG loops was adjusted such that the complete free induction decay (FID) of transverse magnetization was acquired (*i.e.*, $T_2$ decay mechanisms prevented any further detectable refocusing of the signal). The experimental settings corresponded to a spikelet separation of *ca.* 9.5 kHz in the frequency domain.

$^{91}$Zr solid-state NMR spectra of UiO-66_Ac30 and UiO-66_Ac30 (heat treated) samples were also recorded at 35.2 T using static QCPMG experiments. Central transition (CT) selective π/2 and π pulse lengths of 1.4 and 2.8 μs, respectively, were used. Spectra were obtained at three and five offsets (separated by *ca.* 75.5 kHz) for UiO-66_Ac30 and UiO-66_Ac30 (heat treated), respectively, using the VOCS (variable offset cumulative spectra) acquisition method[59] to ensure uniform excitation of the $^{91}$Zr NMR spectra. The QCPMG spikelet separation was set to be *ca.* 6.3 kHz.

Solid-state $^{91}$Zr NMR spectra at 19.6 T ($\nu_0(^{91}\mathrm{Zr})$ = 77.3 MHz) were also recorded at the NHMFL. A Bruker Avance console and a home-built wide-line probe were used, with all MOF samples packed into a 4 mm MAS rotor. Static $^{91}$Zr NMR spectra were obtained using the QCPMG sequence with a 90° pulse length of 2.0 μs. More detailed acquisition parameters for each MOF are shown in Table S1 (ESI†).

Additional details on $^{13}$C and $^{1}$H NMR experiments can be found in SI, and the corresponding spectra are shown in Fig. S2–S7 (ESI†).

### Theoretical calculations

All calculations were performed on SHARCNET computational clusters (**https://www.sharcnet.ca/**). The CASTEP software package[60] was used to perform *ab initio* plane-wave density functional theory (DFT) calculations of $^{91}$Zr EFG tensor parameters. Perdew, Burke, and Ernzerhof (PBE) functionals[61] and the generalized gradient approximation (GGA) for the exchange correlation energy were used in all instances, along with a plane-wave basis set cutoff energy of 800 eV. Calculations employed "on-the-fly" ultrasoft pseudopotentials[62] and the gauge-including projector-augmented wave (GIPAW)[63] formalism. The crystal structures were taken from the Cambridge Crystallographic Data Centre (CCDC) dataset and subjected to geometry optimization using CASTEP; settings included a total energy convergence tolerance of $1 \times 10^{-5}$ eV per atom, a maximum ionic force tolerance of 0.03 eV Å$^{-1}$, a maximum ionic displacement tolerance of 0.001 Å, and a maximum stress component tolerance of 0.05 GPa. To assess the accuracy of the plane-wave DFT approach for $^{91}$Zr NMR parameters, calculations were performed for a series of simple compounds in which the $^{91}$Zr NMR parameters had previously been experimentally determined (Fig. S8 and Table S2, ESI†). Visualization of the EFG tensors produced from CASTEP calculations was performed using the MagresView code.[64]

To address fractional occupancy sites in a crystal structure, one can generate a series of potential structural models based on the different possible atomic arrangements at defined positions within the unit cell or supercell.[65] When fractional occupation issues lead to a large number of possible configurations (*e.g.*, solvent positions in a MOF), calculations and the accompanying analyses become extremely challenging. To investigate the impact of solvent molecules in MOFs, DFT calculations on isolated molecular clusters ("cluster model" DFT calculations) were employed. Cluster model DFT calculations were performed using the Gaussian 16 software package[66] and the B3LYP method. The Zr basis set consisted of a (17s13p9d) configuration contracted to [12s9p5d], with two sets of diffuse p functions ($\alpha_p$ = 0.11323 and 0.04108) and one diffuse d function ($\alpha_d$ = 0.0382).[24] The 6-311G** basis set was used for all other atoms. The EFG tensors calculated using the cluster model DFT calculations were visualized using the EFGShield software package.[67]

## Data availability

The data supporting this article have been included as part of the ESI,† including sample preparation, solid-state NMR experimental details, powder XRD patterns, DFT calculations, additional $^{91}$Zr experimental and simulated NMR spectra. Additional data that support the findings of this study are available from the corresponding author upon request.

## Author contributions

W. Z.: conceptualization, investigation, formal analysis, computation, writing, review, editing; B. E. G. L.: writing, review, editing; V. M.: investigation, review, editing; T. A.: investigation, I. H., Y. X., T. W. G.: investigation; A. V.: investigation, review, editing; Z. G., W. H., A. J. R.: resources, funding, review, editing; Y. H.: conceptualization, resources, funding, formal analysis, writing, review, editing.

## Conflicts of interest

There are no conflicts to declare.

## Acknowledgements

Y. H. thanks the Natural Science and Engineering Research Council (NSERC) of Canada for a Discovery Grant. Synthesis of

UiO-66 samples and solid-state NMR experiments (A. V., T. W. G, W. H., A. J. R.) were supported by the U.S. Department of Energy (DOE), Office of Science, Basic Energy Sciences, Materials Science and Engineering Division. The Ames Laboratory is operated for the U.S. DOE by Iowa State University under Contract DE-AC02-07CH11358. This work was made possible by the facilities of the Shared Hierarchical Academic Research Computing Network (SHARCNET: https://www.sharcnet.ca), Compute/Calcul Canada, and the Digital Research Alliance of Canada. The National High Magnetic Field Laboratory is supported by the National Science Foundation through NSF/DMR-1644779 and NSF/DMR-2128556, and the State of Florida.

## References

1 H. Furukawa, K. E. Cordova, M. O'Keeffe and O. M. Yaghi, *Science*, 2013, **341**, 1230444.
2 A. K. Cheetham, T. D. Bennett, F.-X. Coudert and A. L. Goodwin, *Dalton Trans.*, 2016, **45**, 4113–4126.
3 C. Koschnick, M. W. Terban, R. Frison, M. Etter, F. A. Böhm, D. M. Proserpio, S. Krause, R. E. Dinnebier, S. Canossa and B. V. Lotsch, *J. Am. Chem. Soc.*, 2023, **145**, 10051–10060.
4 C. Koschnick, R. Stäglich, T. Scholz, M. W. Terban, A. von Mankowski, G. Savasci, F. Binder, A. Schökel, M. Etter and J. Nuss, *Nat. Commun.*, 2021, **12**, 1–9.
5 S. Tatay, S. Martínez-Giménez, A. Rubio-Gaspar, E. Gómez-Oliveira, J. Castells-Gil, Z. Dong, Á. Mayoral, N. Almora-Barrios, N. M. Padial and C. Martí-Gastaldo, *Nat. Commun.*, 2023, **14**, 6962.
6 D. Massiot, R. J. Messinger, S. Cadars, M. Deschamps, V. Montouillout, N. Pellerin, E. Veron, M. Allix, P. Florian and F. Fayon, *Acc. Chem. Res.*, 2013, **46**, 1975–1984.
7 J. Kümmerlen and A. Sebald, *Organometallics*, 1997, **16**, 2971–2980.
8 P. Florian and D. Massiot, *CrystEngComm*, 2013, **15**, 8623–8626.
9 S. Yuan, J.-S. Qin, C. T. Lollar and H.-C. Zhou, *ACS Cent. Sci.*, 2018, **4**, 440–450.
10 J. Winarta, B. Shan, S. M. Mcintyre, L. Ye, C. Wang, J. Liu and B. Mu, *Cryst. Growth Des.*, 2019, **20**, 1347–1362.
11 J. N. Hall and P. Bollini, *React. Chem. Eng.*, 2019, **4**, 207–222.
12 Y. Feng, Q. Chen, M. Jiang and J. Yao, *Ind. Eng. Chem. Res.*, 2019, **58**, 17646–17659.
13 T. D. Bennett, A. K. Cheetham, A. H. Fuchs and F. X. Coudert, *Nat. Chem.*, 2016, **9**, 11–16.
14 C. He, S. Li, Y. Xiao, J. Xu and F. Deng, *Solid State Nucl. Magn. Reson.*, 2022, **117**, 101772.
15 O. V. Petrov, V. Chlan, J. Rohlíček, J. Demel, J. Veselý and J. Lang, *J. Phys. Chem. C*, 2020, **124**, 12569–12579.
16 P. He, B. E. G. Lucier, V. V. Terskikh, Q. Shi, J. Dong, Y. Chu, A. Zheng, A. Sutrisno and Y. Huang, *J. Phys. Chem. C*, 2014, **118**, 23728–23744.
17 Y. T. A. Wong, V. Martins, B. E. G. Lucier and Y. Huang, *Chem. – Eur. J.*, 2019, **25**, 1848–1853.
18 R. S. K. Madsen, A. Qiao, J. Sen, I. Hung, K. Chen, Z. Gan, S. Sen and Y. Yue, *Science*, 2020, **367**, 1473–1476.
19 R. K. Harris, E. D. Becker, S. M. C. de Menezes, R. Goodfellow and P. Granger, *Pure Appl. Chem.*, 2001, **73**, 1795–1818.
20 J. Meija, T. B. Coplen, M. Berglund, W. A. Brand, P. De Bièvre, M. Gröning, N. E. Holden, J. Irrgeher, R. D. Loss and T. Walczyk, *Pure Appl. Chem.*, 2016, **88**, 293–306.
21 N. J. Stone, *At. Data Nucl. Data Tables*, 2016, **111**, 1–28.
22 B. E. G. Lucier and Y. Huang, *Annu. Rep. NMR Spectrosc.*, 2015, **84**, 233–289.
23 A. Nadol, F. Venel, R. Giovine, M. Leloire, C. Volkringer, T. Loiseau, C. Gervais, C. Mellot-Draznieks, B. Doumert and J. Trébosc, *Chem. Sci.*, 2025, **16**, 69–82.
24 A. J. Rossini, I. Hung, S. A. Johnson, C. Slebodnick, M. Mensch, P. A. Deck and R. W. Schurko, *J. Am. Chem. Soc.*, 2010, **132**, 18301–18317.
25 Z. Yan, C. W. Kirby and Y. Huang, *J. Phys. Chem. C*, 2008, **112**, 8575–8586.
26 O. Pauvert, F. Fayon, A. Rakhmatullin, S. Kramer, M. Horvatic, D. Avignant, C. Berthier, M. Deschamps, D. Massiot and C. Bessada, *Inorg. Chem.*, 2009, **48**, 8709–8717.
27 J. Zhu, Z. Lin, Z. Yan and Y. Huang, *Chem. Phys. Lett.*, 2008, **461**, 260–265.
28 J. Czernek, L. Kobera, L. Havlak, V. Czerneková, J. Rohlíček, J. Bárta and J. Brus, *Chem. Phys. Lett.*, 2020, **738**, 136855.
29 A. F. R. Kilpatrick, N. H. Rees, Z. R. Turner, J.-C. Buffet and D. O'Hare, *Mater. Chem. Front.*, 2020, **4**, 3226–3233.
30 F. H. Larsen, H. J. Jakobsen, P. D. Ellis and N. C. Nielsen, *J. Phys. Chem. A*, 1997, **101**, 8597–8606.
31 F. H. Larsen, J. Skibsted, H. J. Jakobsen and N. C. Nielsen, *J. Am. Chem. Soc.*, 2000, **122**, 7080–7086.
32 J. H. Cavka, S. Jakobsen, U. Olsbye, N. Guillou, C. Lamberti, S. Bordiga and K. P. Lillerud, *J. Am. Chem. Soc.*, 2008, **130**, 13850–13851.
33 C. A. Trickett, K. J. Gagnon, S. Lee, F. Gándara, H. Bürgi and O. M. Yaghi, *Angew. Chem., Int. Ed.*, 2015, **54**, 11162–11167.
34 H. Wu, Y. S. Chua, V. Krungleviciute, M. Tyagi, P. Chen, T. Yildirim and W. Zhou, *J. Am. Chem. Soc.*, 2013, **135**, 10525–10532.
35 Q. Qian, P. A. Asinger, M. J. Lee, G. Han, K. Mizrahi Rodriguez, S. Lin, F. M. Benedetti, A. X. Wu, W. S. Chi and Z. P. Smith, *Chem. Rev.*, 2020, **120**, 8161–8266.
36 D. Yang and B. C. Gates, *ACS Catal.*, 2019, **9**, 1779–1798.
37 L. Valenzano, B. Civalleri, S. Chavan, S. Bordiga, M. H. Nilsen, S. Jakobsen, K. P. Lillerud and C. Lamberti, *Chem. Mater.*, 2011, **23**, 1700–1718.
38 F. Venel, C. Volkringer, O. Lafon and F. Pourpoint, *Solid State Nucl. Magn. Reson.*, 2022, **120**, 101797.
39 Y. Ma, X. Han, S. Xu, Z. Wang, W. Li, I. Da Silva, S. Chansai, D. Lee, Y. Zou and M. Nikiel, *J. Am. Chem. Soc.*, 2021, **143**, 10977–10985.
40 S. Devautour-Vinot, G. Maurin, C. Serre, P. Horcajada, D. P. da Cunha and V. Guillerm, *Chem. Mater.*, 2012, **24**, 2168–2177.
41 J. Tang, S. Li, Y. Su, Y. Chu, J. Xu and F. Deng, *J. Phys. Chem. C*, 2020, **124**, 17640–17647.
42 W.-L. Peng, F. Liu, X. Yi, S. Sun, H. Shi, Y. Hui, W. Chen, X. Yu, Z. Liu and Y. Qin, *J. Phys. Chem. Lett.*, 2022, **13**, 9295–9302.

43 O. M. Yaghi, M. O'Keeffe, N. W. Ockwig, H. K. Chae, M. Eddaoudi and J. Kim, *Nature*, 2003, **423**, 705–714.

44 Z. Chen, S. L. Hanna, L. R. Redfern, D. Alezi, T. Islamoglu and O. K. Farha, *Coord. Chem. Rev.*, 2019, **386**, 32–49.

45 M. A. Porai-Koshits and L. A. Aslanov, *J. Struct. Chem.*, 1972, **13**, 244–253.

46 S. Øien, D. Wragg, H. Reinsch, S. Svelle, S. Bordiga, C. Lamberti and K. P. Lillerud, *Cryst. Growth Des.*, 2014, **14**, 5370–5372.

47 X. Jiang, S. Li, S. He, Y. Bai and L. Shao, *J. Mater. Chem. A*, 2018, **6**, 15064–15073.

48 F. Vasconcelos, S. Cristol, J.-F. Paul, L. Delevoye, F. Mauri, T. Charpentier and G. Le Caër, *J. Phys.: Condens. Matter*, 2013, **25**, 255402.

49 J. Xu, E. S. M. Blaakmeer, A. S. Lipton, T. M. McDonald, Y. M. Liu, B. Smit, J. R. Long, A. P. M. Kentgens and J. A. Reimer, *J. Phys. Chem. C*, 2017, **121**, 19938–19945.

50 B. Ni, W. Sun, J. Kang and Y. Zhang, *J. Phys. Chem. C*, 2020, **124**, 11595–11608.

51 H. Furukawa, F. Gándara, Y. B. Zhang, J. Jiang, W. L. Queen, M. R. Hudson and O. M. Yaghi, *J. Am. Chem. Soc.*, 2014, **136**, 4369–4381.

52 J. Jiang, F. Gándara, Y.-B. Zhang, K. Na, O. M. Yaghi and W. G. Klemperer, *J. Am. Chem. Soc.*, 2014, **136**, 12844–12847.

53 C. A. Trickett, T. M. Osborn Popp, J. Su, C. Yan, J. Weisberg, A. Huq, P. Urban, J. Jiang, M. J. Kalmutzki and Q. Liu, *Nat. Chem.*, 2019, **11**, 170–176.

54 P. Iacomi, F. Formalik, J. Marreiros, J. Shang, J. Rogacka, A. Mohmeyer, P. Behrens, R. Ameloot, B. Kuchta and P. L. Llewellyn, *Chem. Mater.*, 2019, **31**, 8413–8423.

55 G. Wißmann, A. Schaate, S. Lilienthal, I. Bremer, A. M. Schneider and P. Behrens, *Microporous Mesoporous Mater.*, 2012, **152**, 64–70.

56 V. Bon, I. Senkovska, I. A. Baburin and S. Kaskel, *Cryst. Growth Des.*, 2013, **13**, 1231–1237.

57 F. Vermoortele, B. Bueken, G. Le Bars, B. Van de Voorde, M. Vandichel, K. Houthoofd, A. Vimont, M. Daturi, M. Waroquier and V. Van Speybroeck, *J. Am. Chem. Soc.*, 2013, **135**, 11465–11468.

58 Z. Gan, I. Hung, X. Wang, J. Paulino, G. Wu, I. M. Litvak, P. L. Gor'kov, W. W. Brey, P. Lendi, J. L. Schiano, M. D. Bird, I. R. Dixon, J. Toth, G. S. Boebinger and T. A. Cross, *J. Magn. Reson.*, 2017, **284**, 125–136.

59 D. Massiot, I. Farnan, N. Gautier, D. Trumeau, A. Trokiner and J. P. Coutures, *Solid State Nucl. Magn. Reson.*, 1995, **4**, 241–248.

60 S. J. Clark, M. D. Segall, C. J. Pickard, P. J. Hasnip, M. I. J. Probert, K. Refson and M. C. Payne, *Z. Kristallogr. – Cryst. Mater.*, 2005, **220**, 567–570.

61 J. P. Perdew, K. Burke and M. Ernzerhof, *Phys. Rev. Lett.*, 1996, **77**, 3865.

62 J. R. Yates, C. J. Pickard and F. Mauri, *Phys. Rev. B*, 2007, **76**, 024401.

63 C. J. Pickard and F. Mauri, *Phys. Rev. B: Condens. Matter Mater. Phys.*, 2001, **63**, 245101.

64 S. Sturniolo, T. F. G. Green, R. M. Hanson, M. Zilka, K. Refson, P. Hodgkinson, S. P. Brown and J. R. Yates, *Solid State Nucl. Magn. Reson.*, 2016, **78**, 64–70.

65 S. Cadars, A. Lesage, C. J. Pickard, P. Sautet and L. Emsley, *J. Phys. Chem. A*, 2009, **113**, 902–911.

66 M. J. Frisch, G. W. Trucks, H. B. Schlegel, G. E. Scuseria, M. A. Robb, J. R. Cheeseman, G. Scalmani, V. Barone, B. Mennucci, G. A. Petersson and H. H. Nakatsuji, *et al.*, *Gaussian 16*, Gaussian, Inc., Wallingford CT, 2016.

67 S. Adiga, D. Aebi and D. L. Bryce, *Can. J. Chem.*, 2007, **85**, 496–505.